ASSESSMENT OF AN ADAPTIVE ONE-EQUATION TURBULENCE MODEL FOR LEADING EDGE VORTEX FLOWS ON MULTIPLE SWEPT DELTA WINGS

Moritz Zieher¹, Dominik Sedlacek² and Christian Breitsamter³

- ¹Chair of Aerodynamics and Fluid Mechanics, Technical University of Munich, 85748 Garching bei München, moritz.zieher@tum.de
- ²Chair of Aerodynamics and Fluid Mechanics, Technical University of Munich, 85748 Garching bei München, dominik.sedlacek@tum.de
- ³Chair of Aerodynamics and Fluid Mechanics, Technical University of Munich, 85748 Garching bei München, christian.breitsamter@tum.de

Abstract

Eddy-viscosity turbulence models based on the Boussinesq assumption provide the baseline model for computational fluid dynamics simulations of aerospace applications. In the leading edge vortex flow of high-agility aircraft of mid to low-aspect-ratio wings, these models show a deficit in accuracy, where the deviations from real-world flow fields originate in turbulence modeling. Just the possible combinations of angle of attack, angle of sideslip, and control surface deflections at a distinct Mach number call for an enormous amount of computational fluid dynamics simulations in the aircraft design phase. Thus, employing scale-resolving techniques or using more complex turbulence models is not feasible. This study delivers a detailed analysis of an adaptive turbulence model based on the one equation Spalart-Allmaras turbulence model, designed with special emphasis on leading edge vortex flows. The analysis will be conducted for a generic double and triple delta wing configuration, for which numerical data based on the enhanced turbulence model will be compared to results for the original turbulence model and high-fidelity datasets based on delayed-detached-eddy simulations as well as experimental data such as aerodynamic coefficient polars and particle image velocimetry results.

Keywords: turbulence modeling, vortex flows, multiple swept delta wings

1. Introduction

Modern high-agility aircraft are operated at the limits of the flight envelope. Flight at high angles of attack is an inherent part of both offensive and defensive maneuvering in the world of modern fighter aircraft [1]. Aerodynamic and stability characteristics must provide sufficient control power and maneuverability. Moreover, they face contradicting aerodynamic challenges along their envelope since the slender wings have to enable high agile maneuverability at trans- and subsonic speeds while being designed for supersonic cruise [2]. Flow physics effects directly affect the flight mechanics, which influence stability, controllability, and departure resistance at high angles of attack [1]. Accurate tools to asses these aerodynamic needs in detail are thus fundamental to aircraft designers.

Vortical motions make fluid flows fully three-dimensional and complex, where understanding the vortex structures is a prerequisite for flow prediction and control [3]. In the case of slender wings, such as delta wings, the flow separates from the sharp leading edge. It rolls up to a spiral-shaped primary vortex over the wing to induce additional velocities at its upper surface. The extra lift induced by such leading-edge vortices is commonly called "vortex lift" and positively increases the high angle of attack performance of such delta wing configurations [4, 5]. Substantial pressure gradients between the suction peak of the pressure distribution and the leading edges lead to the separation of the boundary layer at already small angles of attack. The detached boundary layer forms a secondary vortex, counter-rotating to the primary vortex [6]. At a certain angle of attack and flow properties

combinations, vortex burst, or vortex breakdown is characterized by a sudden increase in the vortex cross area and a change in the flow structure from jet- to wake-type flow [7]. Vortex breakdown can be a limiting factor on the operating attitude of a slender-winged aircraft and is thus also of great interest [8]. Adding wing strakes may delay vortex breakdown, evolving single delta wings to double and further multi-delta wing configurations [5]. Brennenstuhl et al. conducted a series of low-speed wind tunnel tests of double delta wings commonly used for modern fighter aircraft [9].

Comprehensive research on modern delta wing aerodynamics has been carried out in recent history. Fritz et al. summarize the accomplishments of the Second International Vortex Flow Experiment, where a 65° delta wing with sharp and blunt/rounded leading edges was investigated experimentally [10]. During the Cranked Arrow Wing Projects (CAWAP I&II), various groups performed numerical simulations of the F-16XL aircraft for purposes of code validation and improved understanding of the flight physics of complex interacting vortical flows [11, 12]. Within the scope of the NATO AVT-316 task group, Hövelmann et al. present experimental and numerical investigations on the aerodynamics of a generic triple-delta wing configuration [13]. Further, Pfnür et al. conduct low-speed wind tunnel tests on a generic double and triple delta wing configuration to investigate the vortex interaction aerodynamics [14].

Morton et al. showed that typical Reynolds Averaged Navier-Stokes (RANS) methods are inadequate for capturing the physics of vortex breakdown at high Reynolds numbers, whereas, in contrast, both Detached Eddy Simulation (DES) and streamline curvature correction (SARC) resembled the experimental data very well [15]. The reduction of accuracy of RANS simulations caused by the extensive alteration of turbulent shear flows caused by system rotation or streamline curvature is a well-known phenomenon [16]. However, for many flow conditions and geometry changes, such as during the aircraft design phase, RANS simulations employing eddy-viscosity turbulence models based on the Boussniesq assumption are still state-of-the-art. RANS simulations of separated flows are more costeffective by at least an order of magnitude than the more advanced eddy models [16, 17]. Another aspect of the research has been the extension or correction of eddy viscosity turbulence models to better suit flow problems with system rotation or vortical motions. Based on the idea of the "gyroscopic stability effect" from Knight et al., Spalart et al. proposed a measure of the extra influence on the turbulence of rotating shear layer flows or curved boundary layers [18, 19]. Smirnov et al. adapt this rotation-curvature correction to the shear stress transport model [20]. A streamline curvature correction (SARC) approach by multiplying the production term in the original Spalart-Allmaras (SA) turbulence model by a rotation function is introduced by Shur et al. [16]. Wilcox et al. generalize the second-order closure scheme developed by Wilcox and Traci for curved streamline flows [21]. Two approaches, the "Modified coefficients approach" and the "Bifurcation approach," are explored by Arolla et al. to account for the effects of rotation and curvature [22]. The majority of available rotation corrections are defined while preserving the globality of the fundamental turbulence model. Moioli et al. implement additional source terms into the one equation SA turbulence model [23, 24]. These added terms are controlled by model coefficients and a "so-called" switch factor, which limits the influence of the additional terms only to vortex-dominated flow regions and switches them off in unaffected areas of the flow.

This work will assess the performance of the adaptive turbulence model by Moioli et al. for the two test cases of a generic double and a generic triple delta wing configuration [23]. With the primary objective of improving aerodynamic coefficients such as lift, drag, and moment coefficients, this adaptive turbulence model contributes to a more efficient and effective aerodynamic design process by refining the calculation of forces and moments acting on structures at a relatively low cost compared to higher order numerical tools or experimental investigations.

The improvements of the RANS simulation results increased the accuracy of aerodynamic data. Flow field representation will be elucidated by comparing the results of numerical simulations based on the original Spalart-Allmaras turbulence model, high-fidelity Delayed Detached Eddy Simulation (DDES), and experimental wind tunnel data.

2. Generic Multiple Swept delta wing Platform

The following investigations will consider a double and a triple delta wing configuration with sharp leading edges. The configurations are part of a generic wing-fuselage delta wing platform subject to a joint research program in cooperation with Airbus Defence and Space and the German Aerospace Center. They are embedded in the NATO AVT-316 task group [25]. Several experimental and numerical studies have been conducted for various configurations [13, 14, 26, 27]. The physical wind tunnel models have a fuselage and interchangeable flat plate wings, where each configuration type is also equipped with deflectable control surfaces, e.g., levcons for triple delta wings and slats for double and triple delta wings.

The two configurations included in this study are described by F2 xx7552 STLong LV00 SL00 for the double delta wing and F3 527552 STLong LV00 SL00 FL00 for the triple delta wing, respectively. The most critical geometrical parameters of the two configurations are listed in Table 1. Additionally, the planforms of the configurations are depicted in Figure 1. The designation of the configurations follows the initial convention developed by Airbus Defence and Space. E.g., the platform F3 527552 STLong LV00 SL00 FL00 describes a triple delta wing (F3) with a 52.5° levcon sweep angle φ_1 , a 75° strake sweep angle φ_2 , and a main wing sweep angle of $\varphi_3 = 52.5^{\circ}$. STLong designates the long strake section of the two possible values for l_2 in Table 1, whereas STShort would designate the shorter version. The abbreviations LV, SL, and FL, followed by the number 00, describe the zero deflection angles for the different available control surfaces: levcon (LV), slat (SL), and flap (FL).

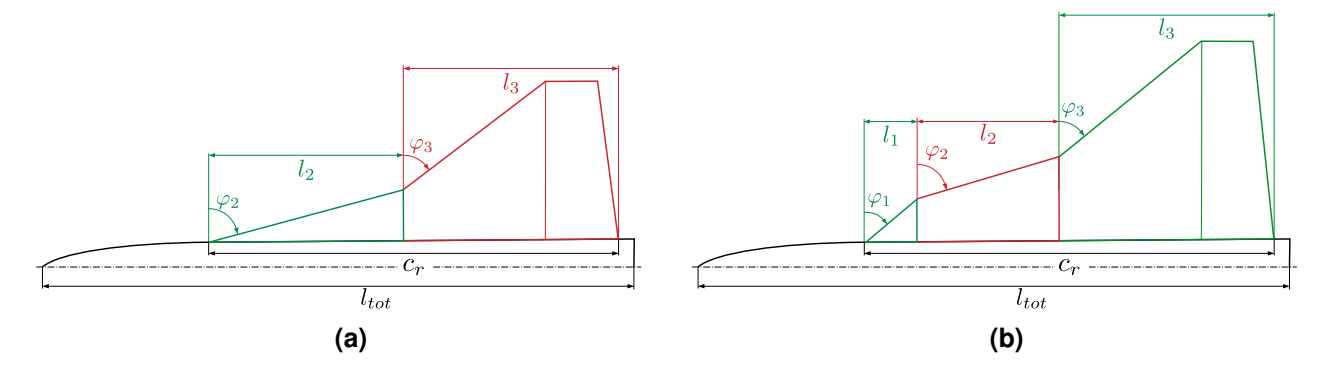


Figure 1 – Generic multiple swept delta wing planforms with corresponding geometrical properties listed in Table 1. (a) Generic double delta wing. (b) Generic triple delta wing.

Table 1 – Geometrical properties for the generic double and triple delta wing configurations (Figure 1).

	Double Delta	Triple Delta
$c_r[m]$	0.625	0.689
s/2[m]	0.366	0.417
$S_{ref} [\mathrm{m}^2]$	0.266	0.329
$\Lambda[-]$	2.02	2.11
$l_{tot}[m]$	1.16	1.16
$l_{\mu}[\mathrm{m}]$	0.426	0.468
$l_1/c_r[-]$	-	0.125
$l_2/c_r[-]$	0.475	0.35
$l_3/c_r[-]$	0.35	0.35
$oldsymbol{arphi}_1$ [°]	-	52.5
$oldsymbol{arphi}_2$ [$^{\circ}$]	75	75
φ ₃ [°]	52.5	52.5

3. Numerical Setup

All simulations are performed with the TAU-Code (triangular adaptive upwind) developed by DLR as the flow solver. Representing not one simple code but a modern software system to compute inviscid and viscous flows at various flow velocities for simple and complex geometries, the DLR TAU-Code is widely accepted in the aviation industry and provides a tool to run complex flow simulations on structured and unstructured hybrid grids. The TAU system comprises different modules and libraries to allow for the easier development, maintenance, and reuse of the code or parts of it. Inter-module communication and interaction with a running simulation is enabled by Python scripting [28].

Flow calculations are based on the dual grid approach, which gives good results for three-dimensional hybrid grids. The Runge-Kutta dual time stepping method or a backward Euler implicit scheme is used as a time-marching method to solve three-dimensional Navier-Stokes equations with LU-SGS (lower-upper symmetric Gauss-Seidel) or SGS iterations. The optimization process described in Section 5. is coupled with TAU via a Python framework (Python 3.8.16).

All simulations are set at a Mach number of $M_{\infty}=0.15$ and a Reynolds number of $Re=3\cdot 10^6$ to resemble the experiments conducted in the wind tunnel of the Chair of Aerodynamics and Fluid Mechanics at the Technical University of Munich by Pfnür et al. [14]. All numerical grids have been designed as hybrid unstructured grids with prism layers, incorporating hexa- and tetraeders with the ANSA pre-processor.

Figure 2 presents the results of the conducted grid study concerning the double delta wing configuration (Figure 1a). Simulations at the angles of attack $\alpha=8^{\circ}$, 16° , 24° , 32° have been run for five different grid resolutions ranging from $\approx 3.4 \cdot 10^6$ grid points for the very coarse (vc) to $\approx 36.5 \cdot 10^6$ grid points for the very fine (vf) grid. Figure 2a indicates that all grid resolutions represent the experimentally obtained lift coefficient rather well. The results of the pitching moment coefficient depicted in Figure 2b show that the deviations from the reference coefficients increase for an increasing angle of attack α . Compared to the other grid resolutions, the fine grid shows an outlier for the pitching moment coefficient in Figure 2b. The source of this pitching behavior of the fine grid could not be discovered. Still, it is noticeable that the outlier is present for all angles of attack except $\alpha=8^{\circ}$ and is not present in the lift coefficient characteristics.

Considering the results of the grid study, the coarse grid resolution was selected. This grid level has $\approx 5.6 \cdot 10^6$ grid points.

4. Adaptive Turbulence Model

Equation 1 gives the enhanced turbulence model formulation based on the original one-equation Spalart-Allmaras Turbulence Model [23, 24]. The additional source terms are controlled by model coefficients and the switch factor ξ (i-vii in Equation 1), which is only effective in vortex-dominated flow regions and switches off the added source terms in the unaffected areas of the flow.

$$\frac{D\tilde{\mathbf{v}}}{Dt} = c_{b1}\tilde{\mathbf{S}}(1 - f_{t2})\tilde{\mathbf{v}} + \frac{1}{\sigma} \left[\nabla \cdot \left((\mathbf{v} + \tilde{\mathbf{v}})\nabla \tilde{\mathbf{v}} \right) + c_{b2}(\tilde{\mathbf{v}})^{2} \right] - \left(c_{w1}f_{w} - \frac{c_{b1}}{\kappa^{2}}f_{t2} \right) \left[\frac{\tilde{\mathbf{v}}}{d} \right]^{2} \\
- \left[\underbrace{c_{bv1}\xi S\tilde{\mathbf{v}} + c_{bv2}\xi^{\frac{1}{2}}S\tilde{\mathbf{v}} + c_{bv3}\xi^{2}S\tilde{\mathbf{v}} + c_{bv4}\left(min\left(\frac{1}{\xi}, c_{vr,lim}\right) \right) \xi_{sw}S\tilde{\mathbf{v}} + c_{bvh1}\xi\tilde{H}\tilde{\mathbf{v}}} \right) \\
+ \underbrace{c_{bvh2} \left[max\left(min\left(\frac{1}{\tilde{H}}, 1.0\right), 0.0 \right) \right] \xi \omega\tilde{\mathbf{v}} + c_{bvb}|\xi\nabla V\omega_{dir}|\tilde{\mathbf{v}}} \right] }$$
(1)

Among all influences, the vortex identifier switch quantity ξ is the most essential control quantity in the adaptive turbulence model. Following the findings of Truesdell and Jeong et al., the vortex identifier quantity is based on the definition that a vortex can be defined as the region where the kinematic vorticity number N_k is greater than one [29, 30]. From the definition $N_k = \omega/S$ and the addition of a

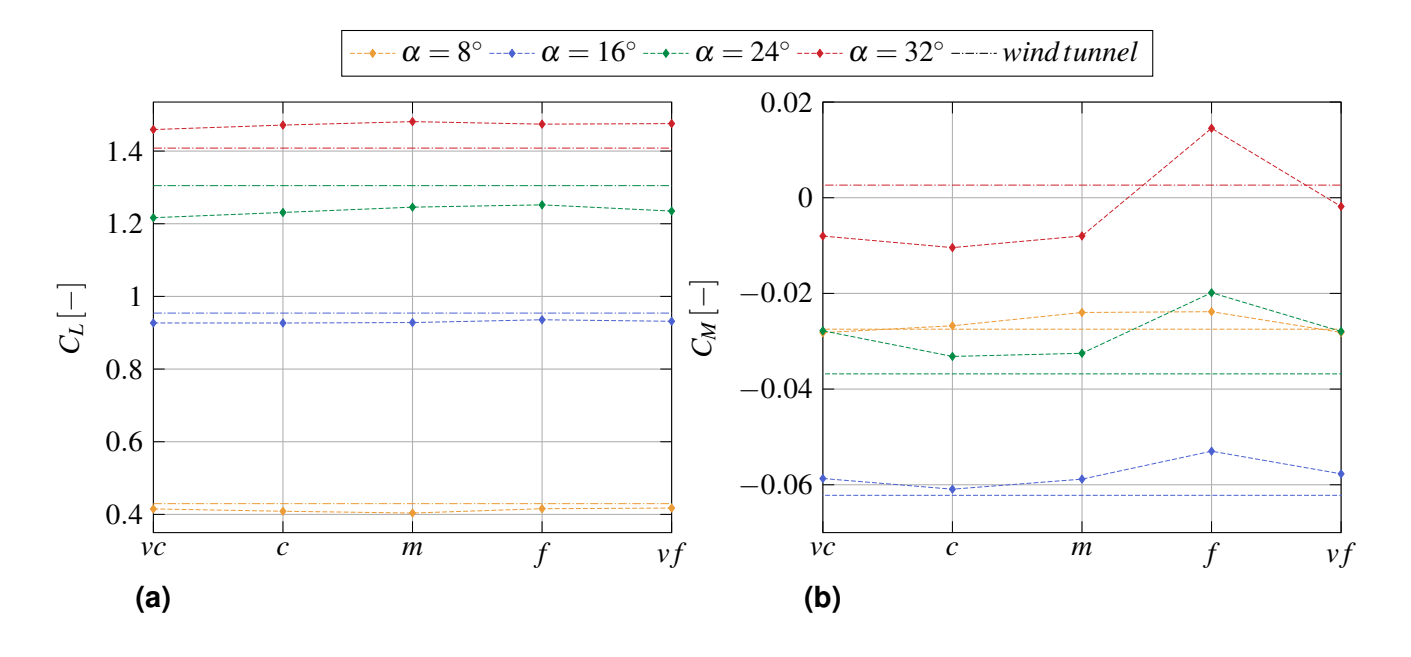


Figure 2 – Gridstudy for the double delta wing configuration (F2 xx7552 STLong LV00 SL00) at Mach number of $M_{\infty}=0.15$, Reynolds number of $Re=3\cdot 10^6$ and angles of attack of $\alpha=[8^{\circ},16^{\circ},24^{\circ},32^{\circ}]$. (a) lift coefficient C_L . (b) pitching moment coefficient C_M .

small number ε to avoid numerical overflow in the case the strain rate takes on values close to zero, the vortex identifier is computed by [23]:

$$\xi = max \left[\left(\left(\frac{\omega}{S + \varepsilon} \right) - c_{vl} \right), 0.0 \right]; c_{vl} = 1$$
 (2)

The coefficient c_{vl} offsets the resulting fraction and is needed to remove the influence of ξ in the boundary layer. The combination of model coefficients, vortex identifier and additional field variables (i - vii in Equation 1) enable the additional source terms to specifically target different vortex-dominated flow subdomains.

Coefficient c_{bv1} (i in Equation 1) controls the term which is most similar to the original coefficient c_{b1} and is only combined with the vortex identifier ξ to introduce additional sources in vortical flow fields. More model flexibility is achieved by introducing two exponentials to ξ (ii - iv in Equation 1). The term c_{bv2} is coupled with a sublinear dependence on ξ by $\xi^{1/2}$, whereas c_{bv3} embodies a superlinear dependency by ξ^2 . The radial-wise influence of the terms is further extended by adding a negative exponent in c_{bv4} to achieve inverse radial influence. Coefficient c_{bvh1} (v in Equation 1) is combined with the normalized helicity \tilde{H} . Expressing the alignment of velocity and vorticity vectors, the helicity $H = V \cdot \omega$ takes on higher values in regions of fully developed vortices since the unburst part of a vortex shows high axial and rotational velocities, where the vorticity is increased along axial direction [31]. Thus, the source term $c_{byh} \xi \tilde{H} \tilde{v}$ acts in regions of fully developed vortices. To prevent the turbulence model from acting differently for right and left-rotating vortices, it is important to use the absolute value of the helicity since the quantity also considers the vortex's chirality [32, 33]. To nondimensionalize all added quantities, the absolute value of helicity is normalized by the free-stream velocity, resulting in a final non-dimensional helicity $\tilde{H} = (V \cdot \omega)/U_{\infty}$. The flow regions downstream of vortex breakdown are influenced by an inverted helicity-based term and the coefficient c_{byh2} . Caused by abrupt changes in rotational and axial velocities, regions of high-velocity gradients can enclose vortex breakdown [8]. Thus, the coefficient c_{bvb} , combined with the velocity gradient tensor and the vorticity direction, mainly influences regions near vortex breakdown. Figure 3 shows the influence of three additional turbulence model coefficients for an exemplary double delta wing configuration.

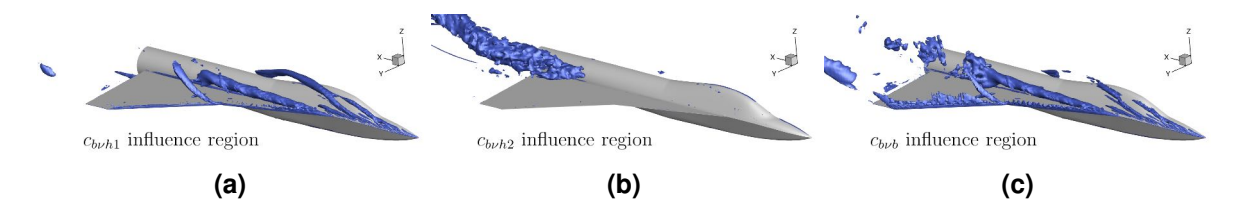


Figure 3 – Influence regions of the additional turbulence model coefficients. (**a**) c_{bvh1} acts on fully developed vortices upstream of vortex breakdown. (**b**) c_{bvh2} influences mainly regions downstream of the vortex breakdown. (**c**) c_{bvb} acts in proximity the vortex breakdown.

5. Optimization of Additional Turbulence Model Coefficients

The additional model coefficients (i - vii) in Equation 1) can be determined by a gradient descent-based optimization process [23]. The iterative algorithm minimizes the L-1 norm between numerical and experimental data $\mathcal{E}(x)$, which is defined as

$$\mathscr{E}(x) = \frac{\sum_{i=1}^{k} \sum_{j=1}^{l} \left[\varepsilon_{exp}^{(i,j)} w_{dp}^{(i)} \right]}{mn \left(\sum_{i=1}^{m} w_{dp}^{(i)} \right)},\tag{3}$$

Where k is the number of design points, e.g., angles of attack, and l is the number of experimental coefficients, e.g., the lift coefficient C_L and pitching moment coefficient C_M . $\varepsilon_{exp}^{(i,j)}$ represents the deviation of numerical from experimental coefficients with the weighting factors $w_{dp}^{(i)}$ controlling the influence of the experimental reference values [23].

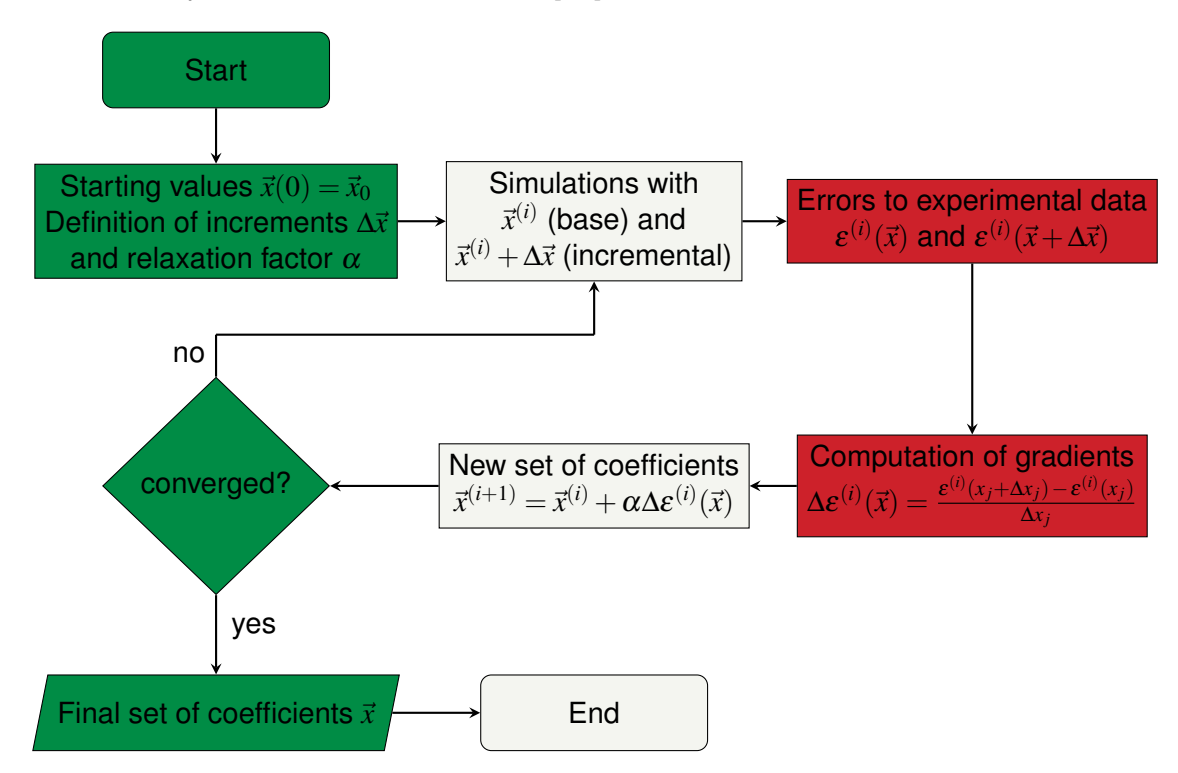


Figure 4 – Flowchart of the coefficient optimization process.

In Figure 4, the optimization process is depicted as a flowchart. First, the user defines a set of start coefficients $\vec{x_0}$ and the increments per model coefficients $\Delta \vec{x}$. Each iteration consists of a first base iteration, after which a simulation with the added coefficient increment is restarted for each active model coefficient. Parallel, a second base simulation is restarted to have a consistent base solution throughout the optimization process. Once all simulations of the current iteration have been concluded, the errors between numerical and experimental reference data can be computed. Based on these errors, the gradients and descent directions are defined and a new set of coefficients is

determined by

$$\vec{x}^{(i+1)} = \vec{x}^{(i)} + \alpha \Delta \varepsilon^{(i)}(\vec{x}), \tag{4}$$

Where $\alpha=0.5$ is used as a relaxation factor to avoid overshooting during the optimization. If the determination of the additional turbulence model coefficient reaches a valuable level of convergence, the optimization concludes with the new set of model coefficients. If the objective function has not converged, the optimization loop is restarted with the recently computed model coefficients as input for the next iteration.

Following this flowchart, in Figure 5, the graph of an optimization run for the double delta wing configuration at $\alpha=24^\circ$ can be seen. In the top part of the figure, the objective function $\mathscr{E}(x)$ is plotted against the optimization iterations. The history of the three active model coefficients of interest is plotted in the lower part of Figure 5.

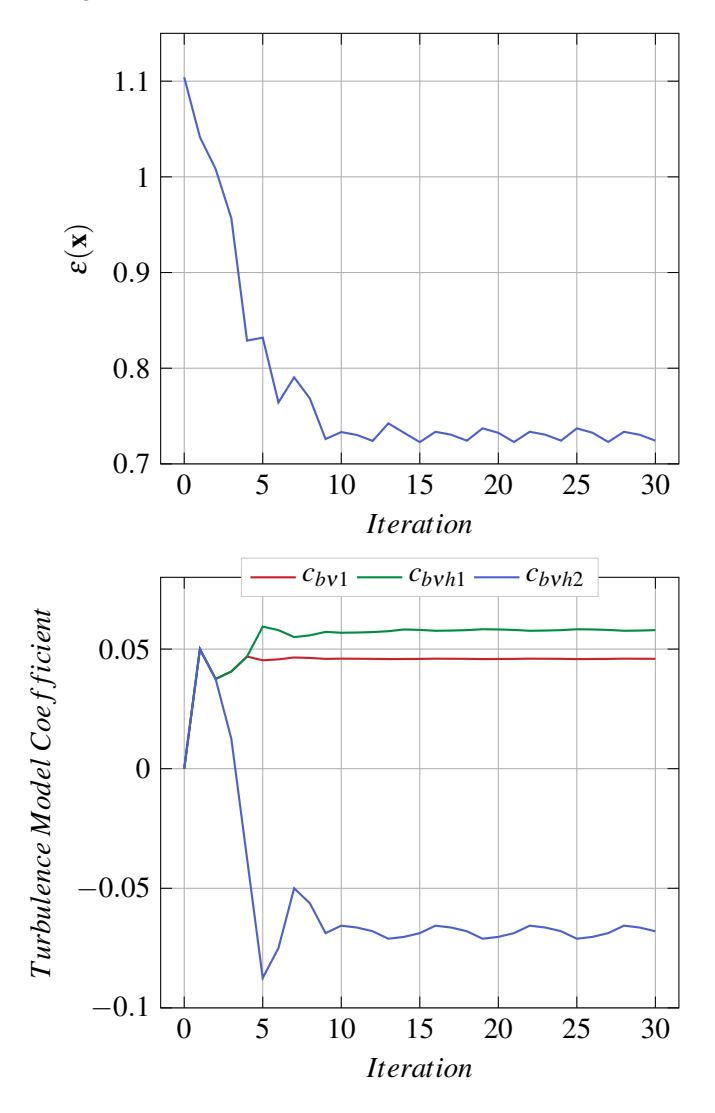


Figure 5 – Sample chart of an optimization process.

6. Results

In the following paragraphs, the results for the double delta wing configuration F2 xx7552 STLong LV00 SL00 and the triple delta wing configuration F3 527552 STLong LV00 SL00 FL00 (Figure 1 & Table 1) are presented. The results are compared between RANS simulations based on the original SA turbulence model with Ewards-modification (SAE), the introduced adaptive turbulence model with

optimized coefficients (SAopt), high-fidelity DDES as well as Particle Image Velocimetry (PIV) wind tunnel results.

Reference PIV data was obtained in the wind tunnel of the Chair of Aerodynamics and Fluid Mechanics at the Technical University of Munich by Pfnür et al. [14]. Already existing high-fidelity DDES results by Sedlacek et al. are taken as further reference [34]. Time-averaged variables are presented for a proper comparison with quasi-steady RANS simulations. For example, the pressure coefficient $\overline{C_P}$ corresponds to the mean pressure coefficient $\overline{C_P}$.

In Table 2, the final set of optimized turbulence model coefficients are listed per angle of attack α and configuration. Since the optimization process is an inherently local approach, this set of coefficients may represent a local rather than a global optimum [23]. Multiple optimization runs with varying starting values would be needed to learn about the local and global minima.

Table 2 – Results of the optimized set of turbulence model coefficients per configuration (**DD** - double delta wing, **TD** - triple delta wing).

	configuration	c_{bv1}	c_{bvh1}	c_{bvh2}	c_{bvb}
$lpha=24^\circ$	DD TD		0.105 0.134	-0.088 0.004	0.089 -0.022
$\alpha = 32^{\circ}$	DD TD	0.273 0.533	0.5 0.393	0.127 0.25	0.515 0.386

6.1 Double delta wing - F2

6.1.1 Aerodynamic Coefficients

In Table 3, the total aerodynamic coefficients are listed for the wind tunnel results and the two different RANS turbulence models. Generally, RANS turbulence models show more problems correctly representing the pitching moment coefficient C_M than the lift coefficient C_M [26].

Comparing the lift coefficient C_L at an angle of attack of $\alpha=24^\circ$, it can be seen that both RANS turbulence models underestimate the absolute lift coefficient. The adaptive turbulence model SAopt improves the error about 1.7%, but both models are relatively close in accuracy. The results for the pitching moment coefficient show that the adaptive turbulence model reduces the percentage error by about 7%.

At an angle of attack of $\alpha=32^\circ$ the resulting lift coefficient improves with the adaptive RANS model, which reduces the error about 4% to nearly 0. Shown by Pfnür et al., the double delta wing configuration exhibits an aggressive and abrupt effect of vortex breakdown, including a severe pitch-up tendency [14]. With a measured maximum lift coefficient at $\alpha_{max}=33^\circ$, the used design point $\alpha=32^\circ$ represents the sign change from nose-down to nose-up pitching moment in the pitching moment slope. At this stage, from a flight dynamics view, critical area of interest, the adaptive RANS reduces the deviation of the pitching moment coefficient by roughly 430%.

6.1.2 Surface Pressure Distribution

The surface pressure distributions on the wing upper side in Figure 6 highlight each simulation result's near-wall flow characteristics.

Comparing the C_P distributions for $\alpha=24^\circ$ (Figure 6a - Figure 6c) it can be deducted, that SAopt slightly reduces the suction peak at the 75° swept strake section. Further, the suction peak area on the main wing is extended downstream when compared to the DDES result in Figure 6c. These changes in the surface pressure distribution contribute to the reduced nose-down pitching moment coefficient discussed in Section 6.1.1

Table 3 – Comparison of the aerodynamic coefficients of experimental and numerical data for the double delta wing configuration at Mach number of $M_{\infty}=0.15$, Reynolds number of $Re=3\cdot 10^6$ and angles of attack of $\alpha=[24^{\circ},32^{\circ}]$.

		C_L	$\Delta C_L[\%]$	C_M	$\Delta C_M[\%]$
$lpha=24^\circ$	experimental SAE SAopt	1.30487 1.23112 1.2537	- 5.65 3.92	-0.03682 -0.03318 -0.03776	9.87 2.56
$\alpha=32^{\circ}$	experimental SAE SAopt	1.40816 1.47157 1.3972	- 4.50 0.78	0.00264 -0.01042 0.00419	- 495.22 58.86

At $\alpha=32^\circ$ (Figure 6d - Figure 6f), the suction peak is shifted downstream from left to right. While the DDES result only shows a moderate negative surface pressure coefficient in the area around the wing kink, both RANS models further extend the negative surface pressure zone downstream on the main wing. Figure 6b shows that the surface pressure coefficient for SAopt gradually rises downstream, while Figure 6a shows that the SAE model results in another distinct suction peak downstream of the kink on the main wing.

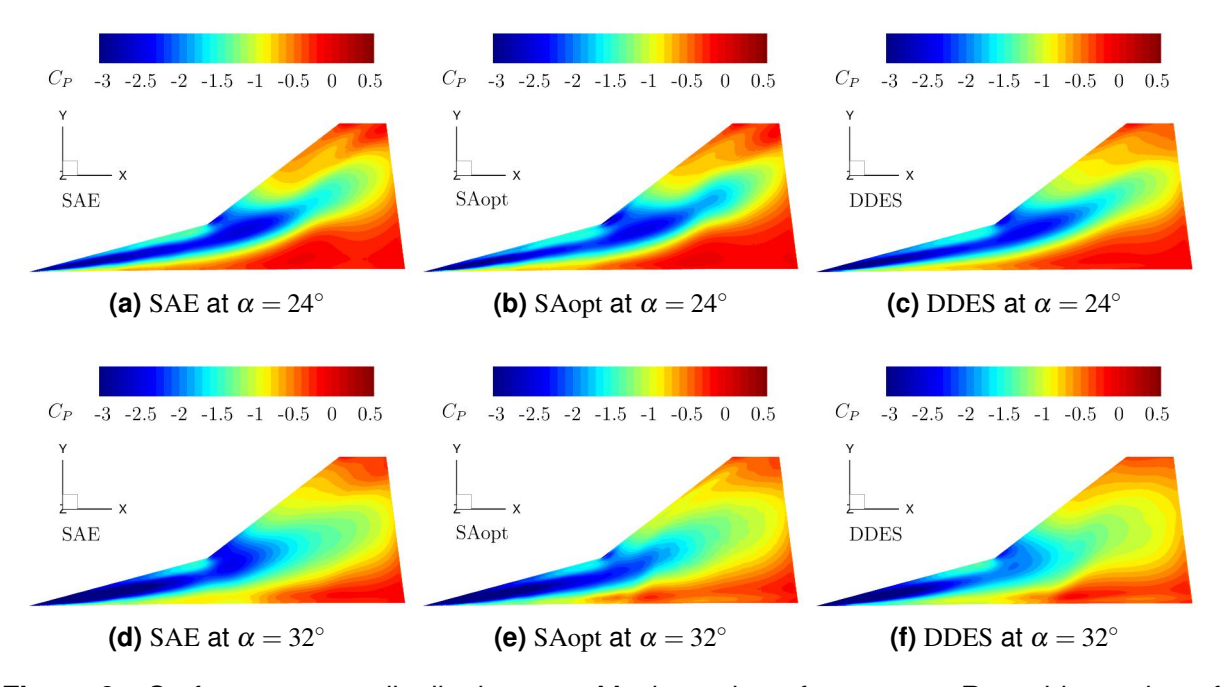


Figure 6 – Surface pressure distribution C_P at Mach number of $M_\infty = 0.15$, Reynolds number of $Re = 3 \cdot 10^6$ and angles of attack of $\alpha = [24^\circ, 32^\circ]$. (a) & (d) SA with Edwards-modification SAE. (b) & (e) adaptive turbulence model SAopt. (c) & (d) averaged high-fidelity DDES.

6.1.3 Vortex Systems

In this subsection, the vortical flow field is examined using an isosurface that represents a 2% total pressure loss $(p_t-p_{t,\infty})/p_{t,\infty}$. This is shown in Figure 7 for the angles of attack of $\alpha=24^\circ$ and $\alpha=32^\circ$. The isosurface is colored according to the non-dimensional axial velocity u/U_∞ . Consistent with the previous section, SAE is pictured on the left-hand side, SAopt in the middle, and DDES on the right-hand side.

Comparing the results for $\alpha=24^\circ$ of both RANS models with the DDES, it can be seen that both delay the expansion of the jet-type vortex core to a wake-type vortex, where SAopt slightly moves the expansion upstream. Further, the inboard vortex (IBV) is more compressed and carries higher

axial core velocities for SAopt. Additionally, the development of the mid-board vortex (MBV) is more pronounced for SAopt and thus alters the interaction on the wing upper side with the IBV.

The $\alpha=32^\circ$ simulation results show similar behavior of the RANS turbulence models. Both models overestimate the strength of the IBV at the strake section. It is to highlight that contrary to Pfnür et al. findings, the DDES predicts the onset of vortex breakdown too far upstream since experimental data suggest that the IBV breaks approximately at the kink [14]. Both RANS models show an expansion of the jet-type vortex around the kink. Still, due to the additional turbulence model coefficients, SAopt better represents the abrupt change of high axial velocities and shows a quick expansion.

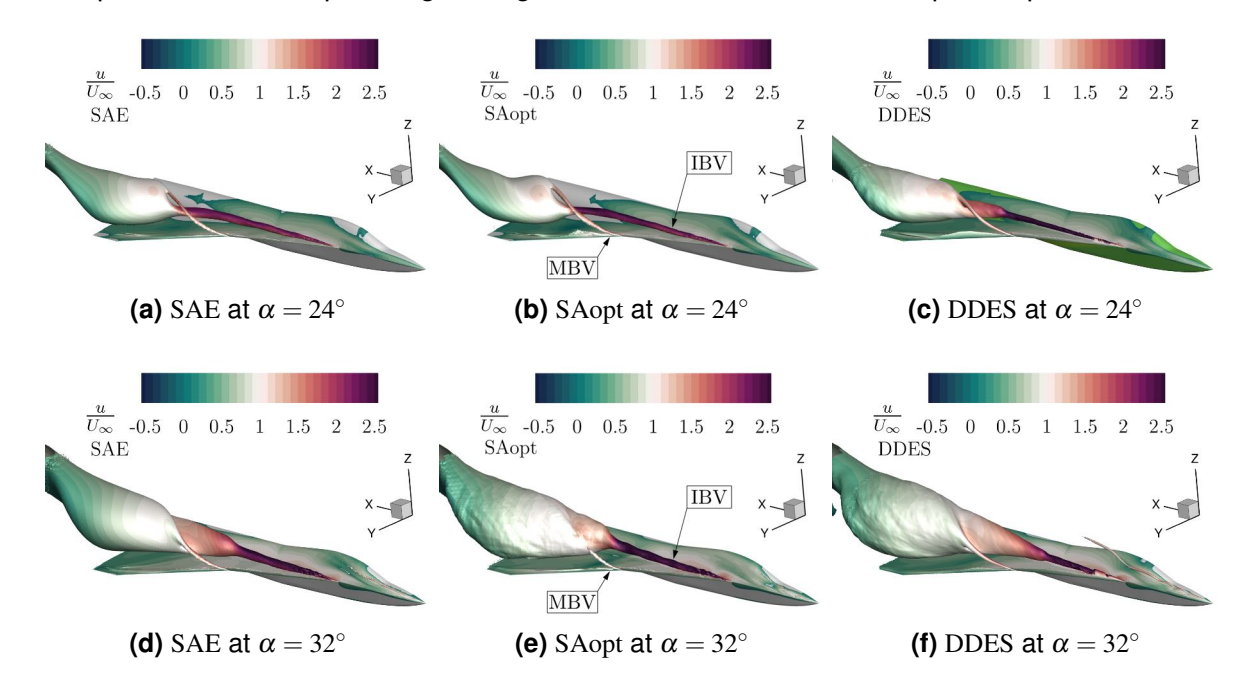


Figure 7 – Vortex flow system visualization by an isosurface of 2% total pressure loss $(p_t - p_{t,\infty})/p_{t,\infty}$ at Mach number of $M_\infty = 0.15$, Reynolds number of $Re = 3 \cdot 10^6$ and angles of attack of $\alpha = [24^\circ, 32^\circ]$. (a) & (d) SA with Edwards-modification SAE. (b) & (e) adaptive turbulence model SAopt. (c) & (d) averaged high-fidelity DDES.

6.1.4 Non-dimensional Axial Vorticity Distribution

In the following, the interaction of the different vortices (IBV & MBV) will be analyzed utilizing the non-dimensional axial vorticity distributions $\omega_x l_\mu/U_\infty$ in selected YZ-cross-section. Simulation results for SAE (left) and SAopt (mid) will be compared with PIV results (right) in the cross-sections positioned downstream of the apex at $x/c_r = [0.317, 0.475, 0.592, 0.708]$, where $x/c_r = 0.475$ represents the wing kink from the 75° swept strake section to the 52.5° swept main wing.

In Figure 8, data for $\alpha=24^\circ$ is depicted. Looking at the first two cross-sections at $x/c_r=0.317$ and $x/c_r=0.475$, SAopt shows similar levels of non-dimensional axial vorticity for the IBV like the PIV results. Especially at the position at the wing kink, SAE shows strongly diminished levels of axial vorticity. Moving downstream of the kink to $x/c_r=0.592$, the development of the MBV can be seen. The SAE model still shows lower axial vorticity levels at this cross-section compared to PIV data. In contrast, the SAopt model shows higher dissipation than the experimental data, resulting in lower non-dimensional axial vorticity levels than the two upstream cross-sections.

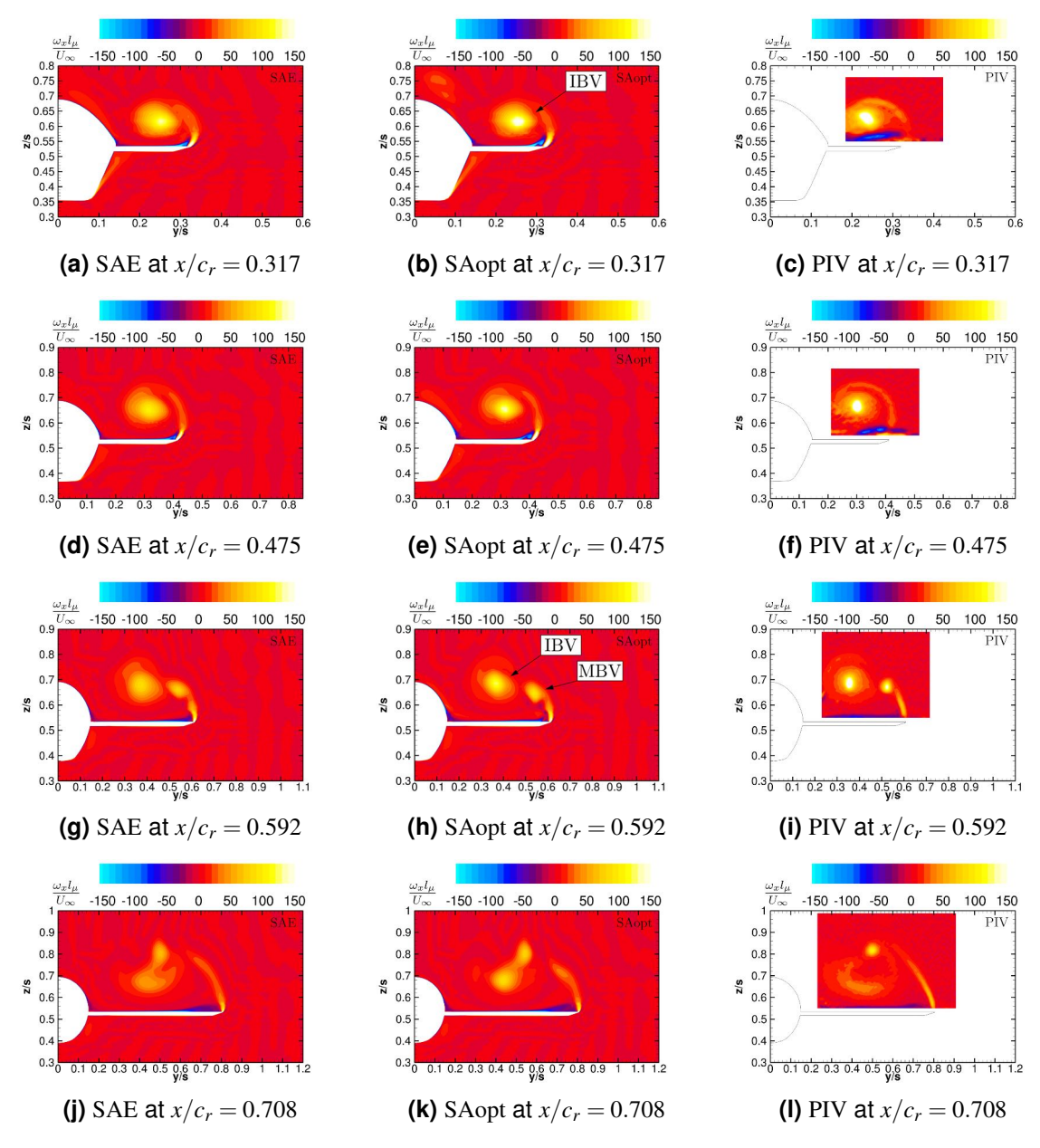


Figure 8 – Cross-section planes of non-dimensional axial vorticity $\omega_x l_\mu/U_\infty$ at Mach number of $M_\infty=0.15$, Reynolds number of $Re=3\cdot 10^6$ and angle of attack of $\alpha=24^\circ$. (a), (d), (g) & (j) SA with Edwards-modification SAE. (b), (e), (h) & (k) adaptive turbulence model SAopt. (c), (f), (i) & (l) averaged quantity of experimental PIV.

At $\alpha=32^\circ$ (Figure 9), both RANS models show similar non-dimensional axial vorticity levels compared to the PIV data in the cross-section at $x/c_r=0.317$. Progressing downstream to $x/c_r=0.475$, the already discussed behavior of overestimating the IBV for SAopt is visible in detail. While experimental data showed that the IBV breaks slightly upstream of the kink at $x/c_r=0.475$, SAopt still indicates a high rotational axial vorticity profile, mispredicting the downstream position of vortex breakdown. The SAE model also shows some rotational flow patterns, but the level of the non-dimensional axial vorticity is comparably lower than for the SAopt model. The cross-section $x/c_r=0.592$ shows that the MBV of SAopt develops at similar axial vorticity magnitudes compared to the PIV MBV, but since there is still a weak IBV present the MBV is influenced by the vortex and moves upwards in the positive z-direction, contrary to the PIV MBV-position. Although the position of the MBV for the SAE model is similar to PIV, the strength of the vortex exceeds experimental data. The most downstream cross-section at $x/c_r=0.708$ shows for all three datasets that the MBV experienced vortex breakdown, and no rotational flow field is present at the downstream part above the main wing.

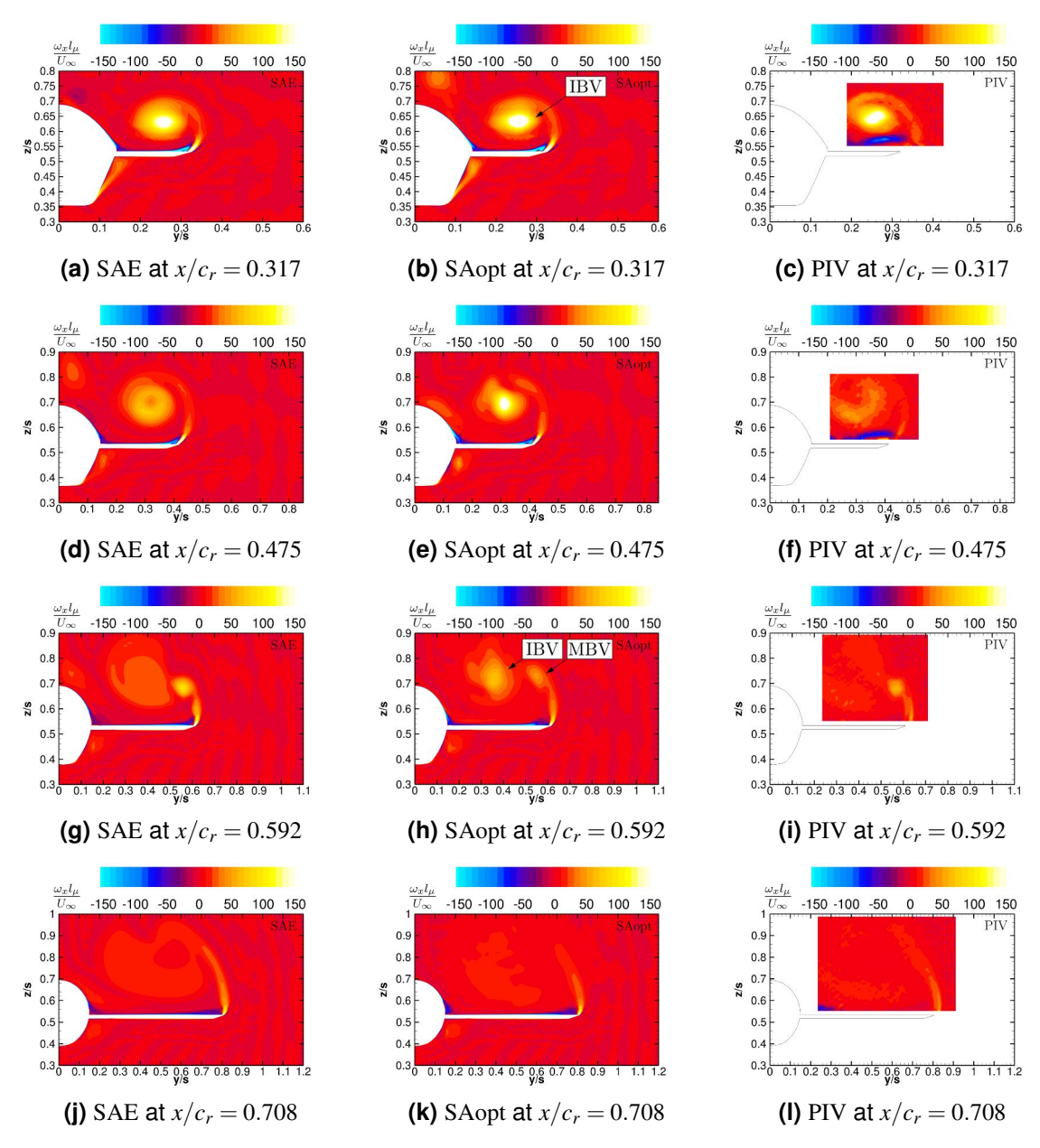


Figure 9 – Cross-section planes of non-dimensional axial vorticity $\omega_{x}l_{\mu}/U_{\infty}$ at Mach number of $M_{\infty}=0.15$, Reynolds number of $Re=3\cdot 10^{6}$ and angle of attack of $\alpha=32^{\circ}$. (a), (d), (g) & (j) SA with Edwards-modification SAE. (b), (e), (h) & (k) adaptive turbulence model SAopt. (c), (f), (i) & (l) averaged quantity of experimental PIV.

6.1.5 Vortex Breakdown

A more detailed view of the differences in the vortex breakdown behavior is given in Figure 10. The rotational flow field is visualized following the definition of Hunt et al. and Kolar et al. that a vortex can be defined as the connected fluid region where the second invariant of the velocity gradient is positive [35, 36].

In Figure 10, isosurfaces of the non-dimensional Q-criterion $Q^* = (Q \cdot l_{\mu}^2)/U_{\infty} = 50$ are shown in green, including stagnating or reversed flow indicated by a red isosurface representing $u/U_{\infty} \leq 0$. For $\alpha = 24^{\circ}$ it was shown in Figure 8 that both RANS models indicate similar behavior to the experimental data and in Figure 10 it can be seen that also the DDES data shows more or less the same breakdown position.

At $\alpha=32^{\circ}$, it can be seen that for the DDES, the red-colored retarded flow region reaches upstream the natural breakdown position at the kink. Further, both RANS models show similar reversed flow

structures at comparable positions. Due to the increased vorticity for the SAopt model, the IBV interacts with the nose vortex and pushes it downwards, where it follows a path across the main wing towards the 52.5° swept leading edge similar to the DDES result.

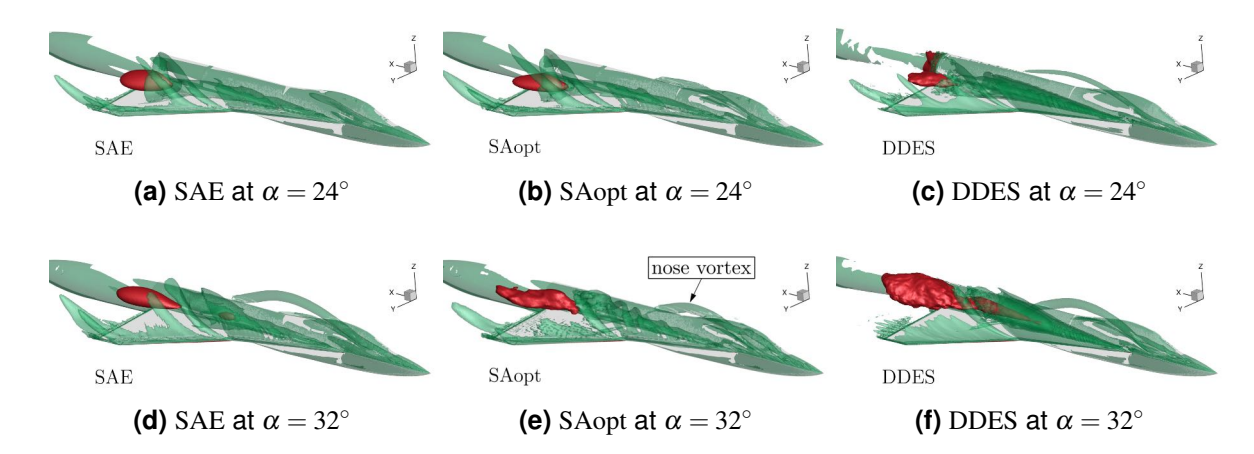


Figure 10 – Vortex breakdown visualization utilizing an isosurface non-dimensional Q-criterion $Q^* = (Q \cdot l_\mu^2)/U_\infty = 50$ (green) and an isosurface of the non-dimensional axial velocity $u/U_\infty < -0.05$ (red) at Mach number of $M_\infty = 0.15$, Reynolds number of $Re = 3 \cdot 10^6$ and angles of attack of $\alpha = [24^\circ, 32^\circ]$. (a) & (d) SA with Edwards-modification SAE. (b) & (e) adaptive turbulence model coefficients SAopt. (c) & (f) averaged high-fidelity DDES.

6.2 Triple delta wing - F3

Similar to the previous sections, the results for the triple delta wing configuration F3 527552 STLong LV00 SL00 FL00 are presented and discussed.

6.2.1 Aerodynamic Coefficients

Table 4 presents the total aerodynamic coefficients for the wind tunnel results and the two distinct RANS turbulence models.

When comparing the lift coefficient C_L at $\alpha=24^\circ$, it is evident that both RANS turbulence models accurately capture the absolute lift coefficient. The adaptive turbulence model SAopt improves the error by approximately 1%, though the accuracy of both models is quite similar. However, the adaptive SAopt model increases the deviation from the experimental value by about 1.5% for the pitching moment coefficient C_M .

At $\alpha=32^\circ$, the results differ significantly. The adaptive RANS model substantially improves the lift coefficient, reducing the error by over 4% to nearly zero. Additionally, the pitching moment coefficient of the SAopt model closely matches the experimental target, while the SAE model shows a significant deviation, with an error of about 12.5%.

6.2.2 Surface Pressure Distribution

Examining the surface pressure distributions on the upper side of the wing in Figure 11, the C_P distributions for $\alpha=24^\circ$ (Figure 11a - Figure 11c) indicate that the SAopt model effectively reduces the intensity of the suction peaks near the junction between the 75° swept strake and the 52.5° swept main wing. The pressure distribution obtained with the SAopt model is more closely aligned with the DDES results than the SAE models.

At $\alpha=32^\circ$ (Figure 11d - Figure 11f), the differences between the two RANS models become more pronounced. The SAopt model exhibits a surface pressure distribution very similar to the DDES result. In contrast, the low-pressure zone for the SAE model extends further downstream across the main wing. Overall, the SAopt model reduces the suction peak across the 52.5° levcon and the 75° swept strake, leading to a reduced nose-up pitching moment, as seen in Table 4.

Table 4 – Comparison of the aerodynamic coefficients of experimental and numerical data for the triple delta wing configuration at Mach number of $M_{\infty}=0.15$, Reynolds number of $Re=3\cdot 10^6$ and angles of attack of $\alpha=[24^{\circ},32^{\circ}]$.

				C_L	$\Delta C_L[\%]$	C_M	$\Delta C_M[\%]$
	$lpha=24^\circ$	experimo SAE SAop		1.28056 1.29672 1.2846	- 1.26 0.32	0.11349 0.10765 0.1060	5.15 6.60
	$\alpha=32^{\circ}$	experime SAE SAop		1.4988 1.5677 1.4934	- 4.60 0.36	0.151012 0.170023 0.1503	- 12.59 0.47
C_P -3 -2.5	-2 -1.5 -1 -0.5	5 0 0.5	Y	-2.5 -2 -1.5	-1 -0.5 0 0	C_P -3 C_P -3 C_P DDES	-2.5 -2 -1.5 -1
(a) SA	AE at $\alpha=24$	4°	(1	b) SAopt at	$\alpha=24^{\circ}$	(c)	DDES at a
C_P -3 -2.5	-2 -1.5 -1 -0.5	5 0 0.5	Y	-2.5 -2 -1.5 x	-1 -0.5 0 0	C_P -3 C_P -3 C_P DDES	-2.5 -2 -1.5 -1

Figure 11 – Surface pressure distribution C_P at Mach number of $M_\infty = 0.15$, Reynolds number of $Re = 3 \cdot 10^6$ and angles of attack of $\alpha = [24^\circ, 32^\circ]$. (a) & (d) SA with Edwards-modification SAE. (b) & (e) adaptive turbulence model SAopt. (c) & (d) averaged high-fidelity DDES.

(e) SAopt at $\alpha = 32^{\circ}$

(f) DDES at $\alpha = 32^{\circ}$

6.2.3 Vortex Systems

(d) SAE at $\alpha=32^{\circ}$

In this subsection, the vortical flow field is analyzed using an isosurface representing a 2% total pressure loss $(p_t-p_{t,\infty})/p_{t,\infty}$. This is illustrated in Figure 12 for angles of attack of $\alpha=24^\circ$ and $\alpha=32^\circ$. The isosurface is colored based on the non-dimensional axial velocity u/U_∞ . Following the previous sections, the results for SAE are shown on the left, SAopt in the middle, and DDES on the right.

Comparing the results for $\alpha=24^\circ$ of both RANS models with the DDES, it is evident that both models closely align with the high-fidelity DDES results. The induced IBV for all three numerical simulations exhibit a similar structure and axial velocity distribution. A slight difference is noted in the MBV development, which is more pronounced in the SAopt model, where the onset of shear layer separation at the 52.5° swept main wing is visible.

For the $\alpha=32^\circ$ simulations, the results, as shown in Figure 11, reveal the already observed differences between the two RANS models. The structure and axial velocity distribution of the IBV for the SAopt model closely match the DDES results. In contrast, the SAE model displays a more compressed jet-like vortex flow with higher axial velocity distribution downstream. Similar to the findings of Pfnür et al., where the MBV travels roughly $\Delta x/c_r \approx 0.1$ before bursting, the MBV in the SAopt

model shows only starting development before merging into the burst IBV region. In contrast, the SAE model exhibits a strongly developed MBV with high non-dimensional axial velocities, extending further downstream towards the rear part of the main wing.

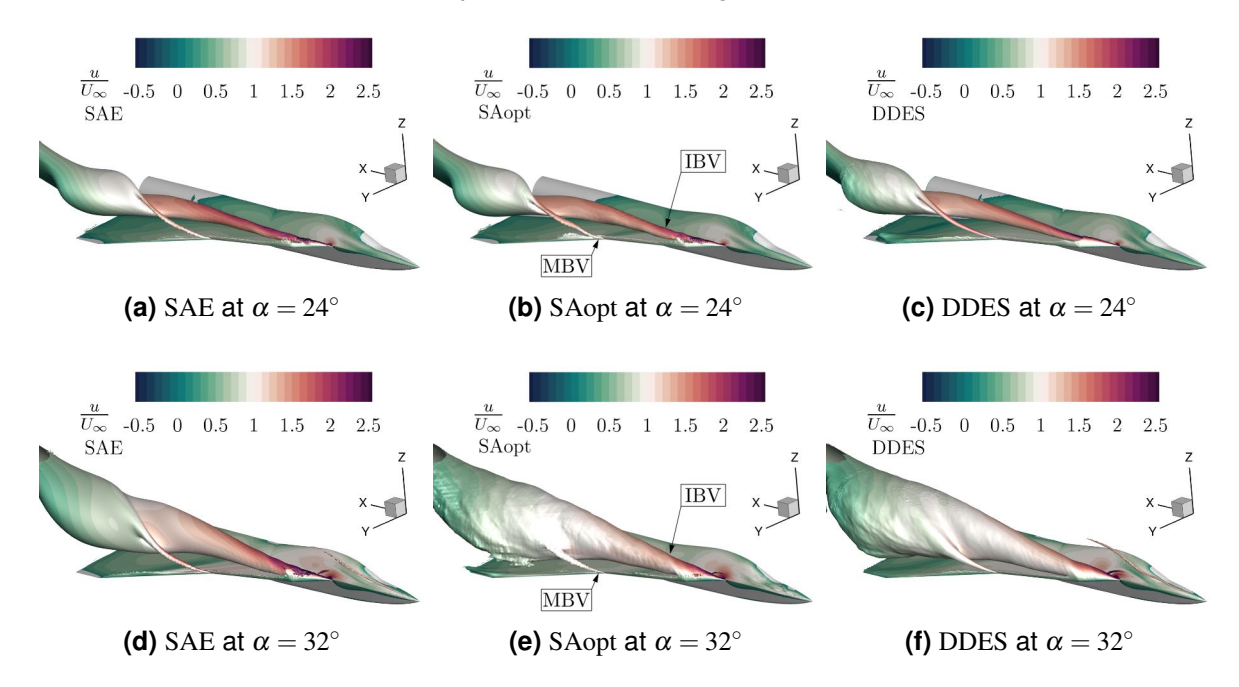


Figure 12 – Vortex flow system visualization by an isosurface of 2% total pressure loss $(p_t - p_{t,\infty})/p_{t,\infty}$ at Mach number of $M_\infty = 0.15$, Reynolds number of $Re = 3 \cdot 10^6$ and angles of attack of $\alpha = [24^\circ, 32^\circ]$. (a) & (d) SA with Edwards-modification SAE. (b) & (e) adaptive turbulence model SAopt. (c) & (d) averaged high-fidelity DDES.

6.2.4 Non-dimensional Axial Vorticity Distribution

The interaction of different vortices (IBV and MBV) will be discussed using the non-dimensional axial vorticity $\omega_x l_\mu/U_\infty$ in selected YZ cross-sections. The simulation results for SAE (left) and SAopt (middle) will be compared with experimental PIV results (right) in the planes positioned downstream of the apex at $x/c_r = [0.242, 0.475, 0.592, 0.708]$, where $x/c_r = 0.475$ marks the transition from the 75° swept strake to the 52.5° swept main wing.

Figure 13 shows the data for $\alpha=24^\circ$. At the first cross-sections located at $x/c_r=0.242$, it is observed that SAopt exhibits similar levels of non-dimensional axial vorticity for the IBV as seen in the PIV results. At the same time, the SAE model displays higher vorticity levels, indicating a stronger IBV. At the next position, $x/c_r=0.475$ at the wing kink, both SAopt and PIV show significantly reduced levels of axial vorticity, with the SAE model also showing diminished levels, closer to the experimental data. Moving downstream to $x/c_r=0.592$, both RANS models exhibit a similar rotational strength for the IBV compared to the PIV results. The development of the MBV is evident, with its strength increasing from left to right. Both RANS models underestimate the MBV, but the SAopt model aligns more closely with the experimental data. At the furthest downstream position, $x/c_r=0.708$, the axial vorticity distribution is similar across the models. Although SAopt represents more accurately the experimental data, it still underestimates the strength of the MBV.

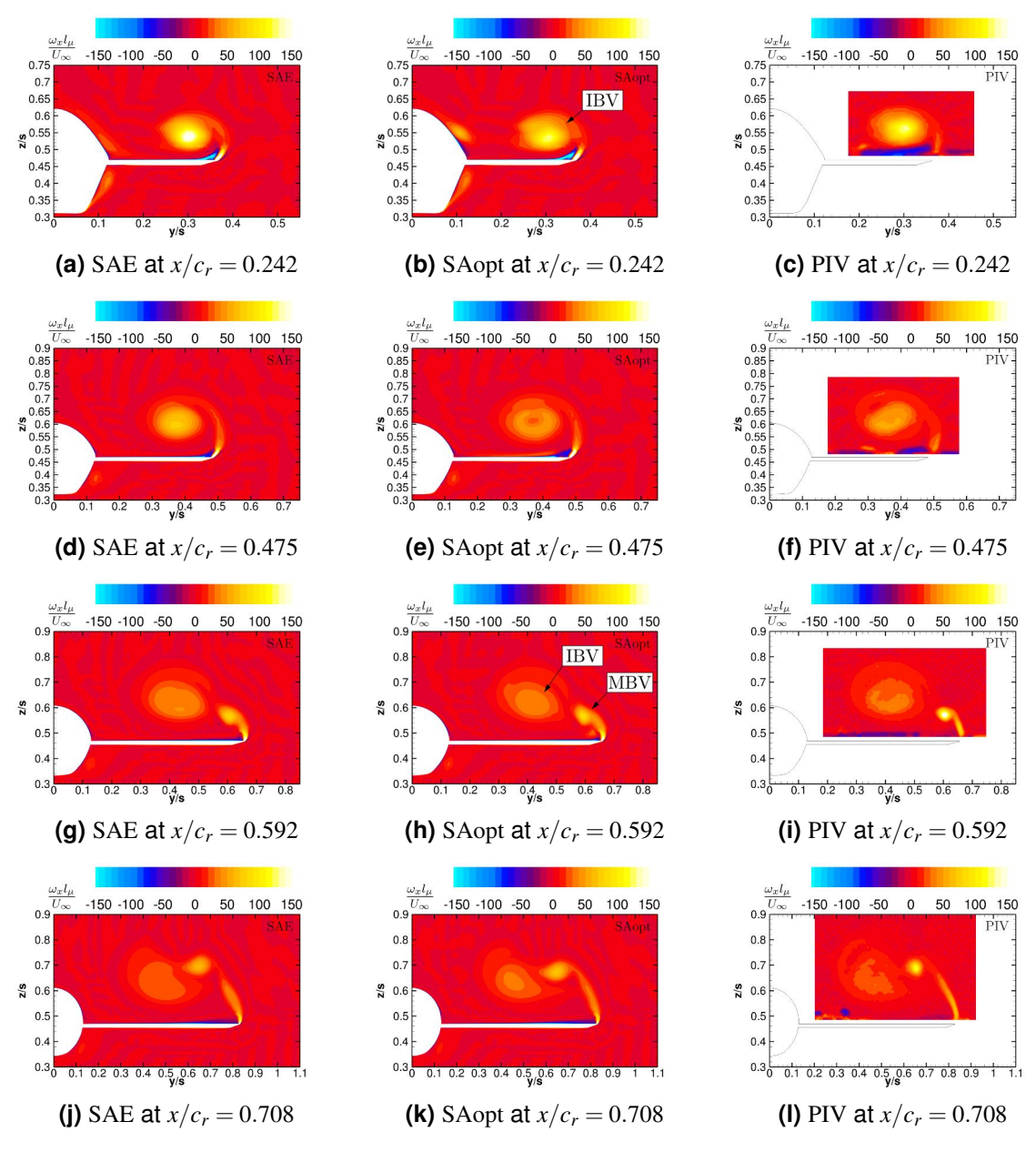


Figure 13 – Cross-section planes of non-dimensional axial vorticity $\omega_x l_\mu/U_\infty$ at Mach number of $M_\infty=0.15$, Reynolds number of $Re=3\cdot 10^6$ and angle of attack of $\alpha=24^\circ$. (a), (d), (g) & (j) SA with Edwards-modification SAE. (b), (e), (h) & (k) adaptive turbulence model SAopt. (c), (f), (i) & (l) averaged quantity of experimental PIV.

At $\alpha=32^\circ$ (Figure 14), the PIV data and the SAopt model in the cross-section at $x/c_r=0.242$ exhibit already reduced levels of non-dimensional axial vorticity, whereas the SAE model shows higher vorticity levels. As seen in Figure 12, the IBV has already burst at the position $x/c_r=0.475$. The SAE model is closer to the other two datasets at this location but still shows a slight rotational flow field. In the cross-section at $x/c_r=0.592$, the SAE model shows some highly rotational MBV, while the SAopt model develops a similar axial vorticity profile to that of the PIV MBV. The most downstream cross-section at $x/c_r=0.708$ indicates that, in all three datasets, the MBV has undergone vortex breakdown, and no rotational flow field is present in the downstream region above the main wing.

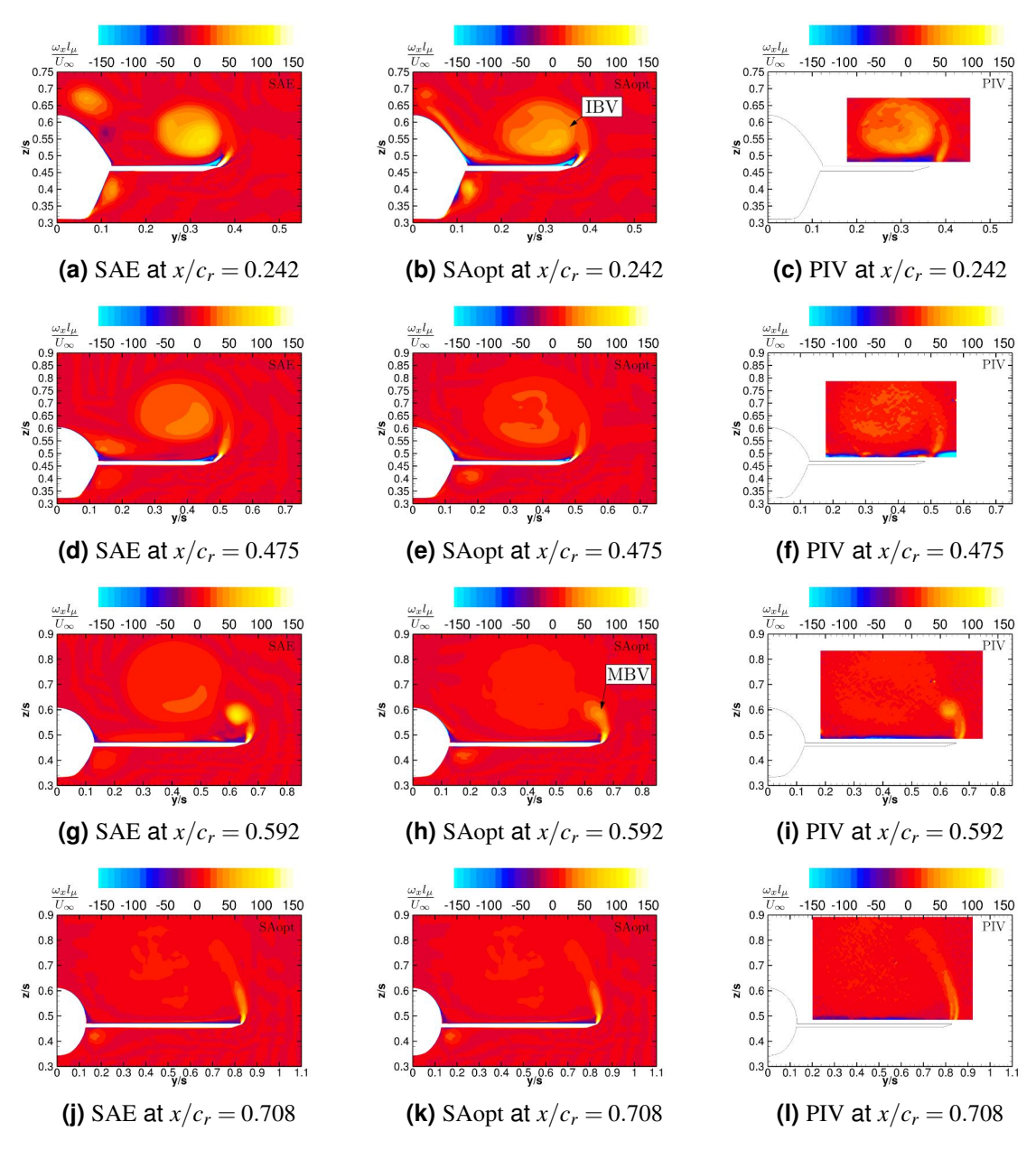


Figure 14 – Cross-section planes of non-dimensional axial vorticity $\omega_x l_\mu/U_\infty$ at Mach number of $M_\infty=0.15$, Reynolds number of $Re=3\cdot 10^6$ and angle of attack of $\alpha=32^\circ$. (a), (d), (g) & (j) SA with Edwards-modification SAE. (b), (e), (h) & (k) adaptive turbulence model SAopt. (c), (f), (i) & (l) averaged quantity of experimental PIV.

6.2.5 Vortex Breakdown

Similar to previous analyses, the differences in vortex breakdown behavior are depicted in Figure 15 using isosurfaces of the non-dimensional Q-criterion $Q^* = (Q \cdot l_{\mu}^2)/U_{\infty} = 50$ in green, and a red isosurface representing stagnating or reversed flow $u/U_{\infty} \leq 0$.

All three numerical models exhibit similar vortical structures across the wing for $\alpha=24^\circ$. Both the SAopt and DDES models display a small reverse flow bubble at the rear part of the wing, which is scarcely present in the SAE model. At $\alpha=32^\circ$, it becomes evident that in the DDES and SAopt models, the red region indicating retarded flow extends upstream towards the apex. This observation is consistent with the findings of Pfnür et al. [14]. Additionally, both models demonstrate similar vortex breakdown positions around the junction between the strake and the main wing, whereas the SAE model shows a delayed breakdown position, extending further downstream.

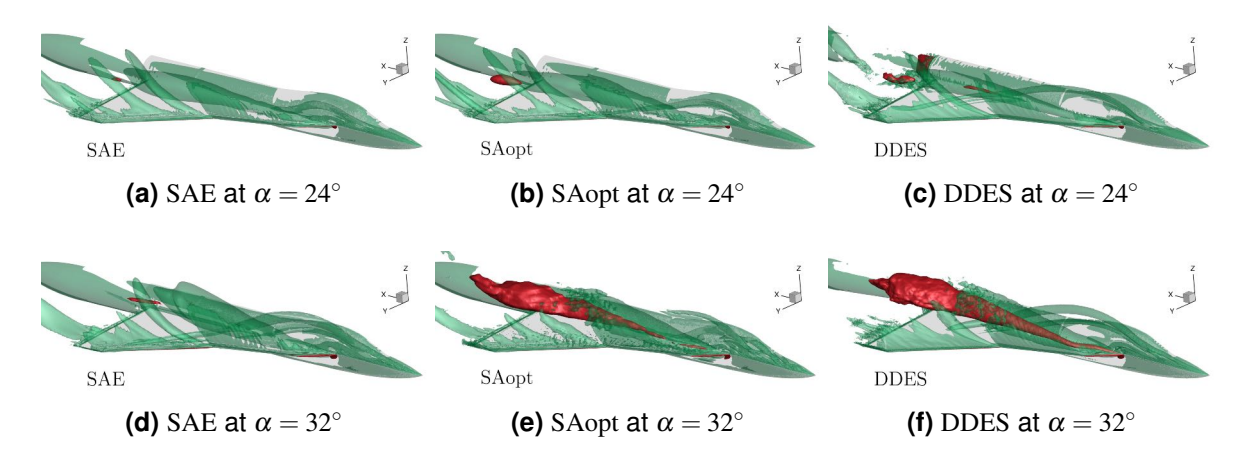


Figure 15 – Vortex breakdown visualization utilizing an isosurface non-dimensional Q-criterion $Q^* = (Q \cdot l_\mu^2)/U_\infty = 50$ (green) and an isosurface of the non-dimensional axial velocity $u/U_\infty < -0.05$ (red) at Mach number of $M_\infty = 0.15$, Reynolds number of $Re = 3 \cdot 10^6$ and angles of attack of $\alpha = [24^\circ, 32^\circ]$. (a) & (d) SA with Edwards-modification SAE. (b) & (e) adaptive turbulence model SAopt. (c) & (d) averaged high-fidelity DDES.

7. Conclusion

This study has extensively evaluated an adaptive turbulence model specifically designed to address the limitations of conventional eddy-viscosity models for simulating leading-edge vortex flows in high-agility aircraft with mid to low-aspect-ratio wings. Built upon the one-equation SA turbulence model, the adaptive turbulence model has been assessed through numerical simulations of generic double and triple delta wing configurations at different angles of attack, with the results benchmarked against high-fidelity datasets from delayed-detached-eddy simulations and empirical data including aerodynamic coefficients and PIV measurements. The findings demonstrate that the adaptive turbulence model significantly enhances the accuracy of CFD simulations for vortex-dominated flow fields, especially at high angles of attack or flight conditions with pronounced vortex breakdown above the wing. The model effectively captures the complex flow phenomena associated with leading-edge vortices, critical to the aerodynamic performance of low aspect-ratio wings, and addresses deficiencies observed in traditional Boussinesq-based eddy-viscosity models.

A vital advantage of the adaptive turbulence model is its ability to provide enhanced predictive capability without the computational burden typically associated with higher-order numerical techniques such as DDES. This balance of improved accuracy and computational efficiency makes it a viable and practical alternative for aerospace design applications, where it is essential to evaluate a vast array of aerodynamic conditions, including varying angles of attack, sideslip, and control surface deflections at distinct Mach numbers. The comparative analysis with the baseline Spalart-Allmaras model and high-fidelity methods confirms the adaptive model's superior performance in capturing the nuanced behavior of leading-edge vortices. This advancement offers a robust framework for improving the fidelity of CFD simulations, thereby supporting the development of more effective and reliable aerodynamic designs.

In conclusion, the adaptive turbulence model represents a significant step forward in turbulence modeling for aerospace applications, providing a more accurate and computationally feasible approach for simulating complex flow fields around low aspect-ratio wings. Future research will aim to extend the applicability of this model to a broader range of aerodynamic conditions and configurations, further enhancing its utility in the iterative process of aircraft design and optimization. Another aspect of the author's research deals with implementing machine learning frameworks to precondition the coefficients of the adaptive turbulence model to add flexibility and scalability. Integrating such advanced turbulence models holds promise for advancing our understanding of aerodynamic phenomena and improving next-generation aircraft overall performance and efficiency.

8. Acknowledgments

The funding of the presented work within the Luftfahrtforschungsprogramm VI-1 (LUFO VI-1) project DIGIfly (FKZ: 20X19091) by the German Federal Ministry for Economic Affairs and Climate Action (BMWK) is gratefully acknowledged. The authors also highly appreciate the supply of comprehensive datasets by Stefan Pfnür.

9. Contact Author Email Address

moritz.zieher@tum.de

10. Copyright Statement

The authors confirm that they, and/or their company or organization, hold copyright on all of the original material included in this paper. The authors also confirm that they have obtained permission, from the copyright holder of any third party material included in this paper, to publish it as part of their paper. The authors confirm that they give permission, or have obtained permission from the copyright holder of this paper, for the publication and distribution of this paper as part of the ICAS proceedings or as individual off-prints from the proceedings.

References

- [1] Skow, A. M., and Erickson, G. E., "Modern fighter aircraft design for high-angle-of-attack maneuvering," High Angle-of-Attack Aerodynamics, AGARD-LS-121, 1982, pp. 4–1–4–49.
- [2] Hitzel, S., "Sub- and Transonic Vortex Breakdown Flight Condition Simulations of the F-16XL Aircraft," Journal of Aircraft, Vol. 54, No. 2, 2017, pp. 428–443. https://doi.org/10.2514/1.c033246.
- [3] Kida, S., and Miura, H., "Identification and analysis of vortical structures," *European Journal of Mechanics B/Fluids*, Vol. 17, No. 4, 1998, pp. 471–488. https://doi.org/10.1016/s0997-7546(98)80005-8.
- [4] Hummel, D., "On the Vortex Formation Over a Slender Wing at Large Angles of Incidence," *High Angle-of-Attack Aerodynamics, AGARD CP-247*, 1978, pp. 15–1–15–17.
- [5] Kohlman, D. L., and Wentz, W. H., "Wind tunnel investigations of vortex breakdown on slender sharp edged wings Final report," *NASA CR-98737*, 1968.
- [6] Hummel, D., "Experimental investigation of the flow on the suction side of a thin Delta wing," NASA-TM-75897, 1981.
- [7] Breitsamter, C., "Unsteady flow phenomena associated with leading-edge vortices," *Progress in Aerospace Sciences*, Vol. 44, No. 1, 2008, pp. 48–65. https://doi.org/10.1016/j.paerosci.2007.10.002.
- [8] Hall, M. G., "Vortex Breakdown," *Annual Review of Fluid Mechanics*, Vol. 4, No. 1, 1972, pp. 195–218. https://doi.org/10.1146/annurev.fl.04.010172.001211.
- [9] Brennenstuhl, U., and Hummel, D., "Vortex formation over double-delta wings," ICAS-82-6.6.3, 1982.
- [10] Fritz, W., and Cummings, R., "Lessons Learned from the Numerical Investigations on the VFE-2 Configuration," *Published in Report: Understanding and Modeling Vortical Flows to Improve the Technology Readiness Level for Military Aircraft*, 2009, pp. 1–34.
- [11] Rizzi, A., Jirásek, A., Lamar, J. E., Crippa, S., Badcock, K. J., and Boelens, O. J., "Lessons Learned from Numerical Simulations of the F-16XL Aircraft at Flight Conditions," *Journal of Aircraft*, Vol. 46, No. 2, 2009, pp. 423–441. https://doi.org/10.2514/1.35698.
- [12] Rizzi, A. W., "What was Learned in Predicting Slender Airframe Aerodynamics with the F16-XL Aircraft," 52nd Aerospace Sciences Meeting, American Institute of Aeronautics and Astronautics, 2014. https://doi. org/10.2514/6.2014-0759.
- [13] Hövelmann, A., Winkler, A., Hitzel, S. M., Richter, K., and Werner, M., "Analysis of Vortex Flow Phenomena on Generic Delta Wing Planforms at Transonic Speeds," *New Results in Numerical and Experimental Fluid Mechanics XII*, edited by A. Dillmann, G. Heller, E. Krämer, C. Wagner, C. Tropea, and S. Jakirlić, Springer International Publishing, Cham, Switzerland, 2019, pp. 307–316. https://doi.org/10.1007/978-3-030-25253-3_30.

- [14] Pfnür, S., Pflüger, J., and Breitsamter, C., "Analysis of Vortex Flow Phenomena on Generic Delta Wing Planforms at Subsonic Speeds," *Notes on Numerical Fluid Mechanics and Multidisciplinary Design*, Springer International Publishing, 2019, pp. 328–337. https://doi.org/10.1007/978-3-030-25253-3 32.
- [15] Morton, S., Forsythe, J., Mitchell, A., and Hajek, D., "DES and RANS simulations of delta wing vortical flows," 40th AIAA Aerospace Sciences Meeting Exhibit, AIAA, 2002. https://doi.org/10.2514/6.2002-587.
- [16] Shur, M. L., Strelets, M. K., Travin, A. K., and Spalart, P. R., "Turbulence Modeling in Rotating and Curved Channels: Assessing the Spalart-Shur Correction," *AIAA Journal*, Vol. 38, No. 5, 2000, pp. 784–792. https://doi.org/10.2514/2.1058.
- [17] Frink, N. T., Murphy, P. C., Atkins, H. L., Viken, S. A., Petrilli, J. L., Gopalarathnam, A., and Paul, R. C., "Computational Aerodynamic Modeling Tools for Aircraft Loss of Control," *Journal of Guidance, Control, and Dynamics*, Vol. 40, No. 4, 2017, pp. 789–803. https://doi.org/10.2514/1.g001736.
- [18] Knight, D., and Saffman, P., *Turbulence model predictions for flows with significant mean streamline curvature*, 1978. https://doi.org/10.2514/6.1978-258.
- [19] Spalart, P., and Shur, M., "On the sensitization of turbulence models to rotation and curvature," *Aerospace Science and Technology*, Vol. 1, No. 5, 1997, pp. 297–302. https://doi.org/10.1016/s1270-9638(97)90051-1.
- [20] Smirnov, P. E., and Menter, F. R., "Sensitization of the SST Turbulence Model to Rotation and Curvature by Applying the Spalart–Shur Correction Term," *Journal of Turbomachinery*, Vol. 131, No. 4, 2009. https://doi.org/10.1115/1.3070573.
- [21] Wilcox, D., and Chambers, T., "Streamline Curvature Effects on Turbulent Boundary Layers," AIAA Journal, Vol. 15, No. 4, 1977, pp. 574–580. https://doi.org/10.2514/3.60662.
- [22] Arolla, S. K., and Durbin, P. A., "Modeling rotation and curvature effects within scalar eddy viscosity model framework," *International Journal of Heat and Fluid Flow*, Vol. 39, 2013, pp. 78–89. https://doi.org/10.1016/j.ijheatfluidflow.2012.11.006.
- [23] Moioli, M., Breitsamter, C., and Sørensen, K. A., "Parametric data-based turbulence modelling for vortex dominated flows," *International Journal of Computational Fluid Dynamics*, Vol. 33, No. 4, 2019, pp. 149–170. https://doi.org/10.1080/10618562.2019.1617857.
- [24] Spalart, P., and Allmaras, S., "A one-equation turbulence model for aerodynamic flows," 30th Aerospace Sciences Meeting and Exhibit, AIAA, 1992. https://doi.org/10.2514/6.1992-439.
- [25] Hitzel, S. M., Winkler, A., and Hövelmann, A., "Vortex Flow Aerodynamic Challenges in the Design Space for Future Fighter Aircraft," *New Results in Numerical and Experimental Fluid Mechanics XII*, Springer International Publishing, 2019, pp. 297–306. https://doi.org/10.1007/978-3-030-25253-3_29.
- [26] Guilmineau, E., and Visonneau, M., "Evaluation of turbulence modelling for subsonic vortex interaction on multi delta wing configuration," *56th 3AF International Conference on Applied Aerodynamics*, Toulouse, France, 2022.
- [27] Visonneau, M., Guilmineau, E., and Wackers, J., "Computational Analysis of Subsonic Vortex Interaction on Multi Swept Delta Wing Configurations," *AIAA SCITECH 2022 Forum*, AIAA, 2022. https://doi.org/10.2514/6.2022-0027.
- [28] Schwamborn, D., Gerhold, T., and Heinrich, R., "The DLR TAU-Code: Recent Applications in Research and Industry," *ECCOMAS CFD CONFERENCE*, 2006, pp. 1–25.
- [29] Truesdell, C., "The physical components of vectors and tensors," ZAMM Journal of Applied Mathematics and Mechanics / Zeitschrift für Angewandte Mathematik und Mechanik, Vol. 33, No. 10–11, 1953, pp. 345–356. https://doi.org/10.1002/zamm.19530331005.
- [30] Jeong, J., and Hussain, F., "On the identification of a vortex," *Journal of Fluid Mechanics*, Vol. 285, 1995, pp. 69–94. https://doi.org/10.1017/s0022112095000462.
- [31] Nelson, R. C., and Visser, K. D., "Breaking down the delta wing vortex: The role of vorticity in the break-down process. Ph.D. Thesis Final Report," 1991.
- [32] Moreau, J. J., "Constantes d'un îlot tourbillonnaire en fluide parfait barotrope," *Comptes rendus hebdomadaires des séances de l'Académie des sciences*, Vol. 252, 1961, pp. 2810–2812.

- [33] Moffatt, H. K., "The degree of knottedness of tangled vortex lines," *Journal of Fluid Mechanics*, Vol. 35, No. 1, 1969, pp. 117–129. https://doi.org/10.1017/s0022112069000991.
- [34] Sedlacek, D., Biechele, S., and Breitsamter, C., "Numerical investigations of vortex formation on a generic multiple-swept-wing configuration," *CEAS Aeronautical Journal*, Vol. 13, No. 1, 2021, pp. 295–310. https://doi.org/10.1007/s13272-021-00566-y.
- [35] Hunt, J., and Studying, s., "Turbulence Using Numerical Simulation Databases," 1988, p. 1.
- [36] Kolář, V., "Vortex identification: New requirements and limitations," *International Journal of Heat and Fluid Flow*, Vol. 28, No. 4, 2007, pp. 638–652. https://doi.org/10.1016/j.ijheatfluidflow.2007.03.004.